REVISION 1

Title: Non-hydrothermal origin of apatite in SEDEX mineralization and host rocks of the Howard's Pass district, Yukon, Canada

Michael G. Gadd[1]*, Daniel Layton-Matthews[1], Jan M. Peter[2]

[1]Department of Geological Sciences and Geological Engineering, Queen's University, 36 Union Street, Kingston, Ontario, Canada K7L 3N6; *email: mggadd3@gmail.com

[2]Geological Survey of Canada, 601 Booth Street, Ottawa, Ontario, Canada K1A 0E8

Abstract

The Howard's Pass district comprises 14 Zn-Pb sedimentary exhalative (SEDEX) deposits and is located within the Selwyn basin, Yukon, Canada. Although the HPD is renowned for its large accumulation of base-metal sulfides, in places the Late Ordovician to Early Silurian host rocks also contain abundant (carbonate-bearing) fluorapatite (CBFA). This mineral is present stratigraphically below, within and above the SEDEX deposits and occurs as fine-grained layers that are interbedded with cherty carbonaceous mudstone. Electron probe microanalysis and laser ablation-inductively coupled plasma-mass spectrometric analysis reveal that mineral compositions and rare earth element-yttrium (REE-Y) systematics, respectively, are remarkably similar throughout the stratigraphic succession. North American Shale Composite (NASC)-normalized La/Sm and La/Yb ratios indicate that the original REE compositions in CBFA have undergone only minor compositional modification subsequent to deposition. Uniformly negative Ce anomalies indicate that the mineral formed in analogous manner to modern and ancient sedimentary phosphorites under suboxic bottom-water conditions. Europium anomalies are mostly absent, indicating that reduced, slightly acidic high-temperature hydrothermal

fluids were not a major source of REE-Y to CBFA. The chemical homogeneity of the mineral irrespective of its stratigraphic position indicates that a common process was responsible for its deposition within the sedimentary rocks of the HPD. On the basis of the similarity of the REE patterns to modern and ancient phosphorites, and the absence of positive Eu anomalies, we conclude that the CBFA is of hydrogenous origin, and not hydrothermal as suggested by previous workers. As such, phosphorite formation in the HPD is casually related to SEDEX Zn-Pb deposit formation.

Keywords: Rare earth element-yttrium, REE-Y, LA-ICP-MS, EPMA, Sedimentary Exhalative Zn-Pb, Apatite

Introduction

Howard's Pass is located within Selwyn basin, Yukon Territory, Canada (Fig. 1A) and comprises a 38 km-long district of 14 Zn-Pb sedimentary exhalative (SEDEX) deposits (Fig. 1B) that are hosted within Late Ordovician to Early Silurian carbonaceous, calcareous to siliceous mudstones. The most notable feature of the Howard's Pass district (HPD) is its large accumulation of base-metal sulfides (400.7 Mt at 4.5% Zn and 1.5% Pb; Kirkham et al., 2012) deposited on the same Early Silurian time-stratigraphic horizon. Another notable feature is the abundance of thinly bedded phosphorites of the immediate host rocks and rocks stratigraphically below and above these deposits. Bedded phosphorites are particularly abundant in the rocks immediately below (<20 m, up to 30 vol.%) and above (20 to 50 m, up to 50 vol.%) the SEDEX deposits, whereas the apatite content is low (up to, but typically less than 10 vol.%) within the deposits (Goodfellow, 1984; Slack et al., 2011).

Apatite is a moderately common mineral in fine-grained carbonaceous sedimentary rocks. This mineral has been interpreted to form at or near the sediment-water interface (e.g., Miocene Monterey Bay Formation; Föllmi et al., 2005), or within the upper part of the sediment pile during early diagenesis (e.g., Peru continental margin; Froelich et al., 1988). Phosphorite deposition (phosphogenesis) in modern sedimentary environments is commonly microbially mediated, where it operates with active communities of sulfate reducing and sulfide oxidizing bacteria (e.g., Peruvian margin; Arning et al., 2009). Apatite is also common in some sediment-hosted metallic mineral deposits (e.g., Zn-Pb Gamsberg deposit, South Africa; Stalder and Rozendaal, 2004). The origin of apatite within the HPD remains controversial. Some workers proposed a link between phosphogenesis and SEDEX deposit formation, whereby phosphorus was delivered together with Zn and Pb in the same hydrothermal fluid from which Zn-Pb mineralization was precipitated (Goodfellow, 1984; Goodfellow, 1999). However, others more recently have hypothesized that apatite formed from constituent elements and authigenic processes unrelated to hydrothermal fluid discharge, such as Fe redox pumping or upwelling of nutrient-rich waters (Johnson et al., 2014; Slack et al., 2011).

Rare earth element-yttrium (REE-Y) compositions are commonly used to elucidate the genesis of apatite and the ambient paleoenvironmental conditions under which this mineral forms (e.g., Garnit et al., 2012; Joosu et al., 2015; Lécuyer et al., 2004; Picard et al., 2002; Reynard et al., 1999). Cerium and Eu are particularly useful because their abundances are controlled by redox conditions and they can be fractionated from the other REE under oxidizing or reducing environmental conditions. Paleoenvironmental redox conditions (i.e., highly reducing) are implicated as a

fundamental control for the timing, formation and preservation of SEDEX deposits (e.g., Goodfellow, 1987; Turner, 1992). Indeed, these workers hypothesize euxinic (i.e., reducing and sulfidic) ambient water conditions as the primary source of sulfur in SEDEX deposits. However, recent work in the HPD (Gadd et al., 2015a; Gadd et al., 2015b) and in other sediment-hosted base-metal districts (e.g., MacMillan Pass, Magnall et al., 2015; Red Dog, Reynolds et al., 2015) shows that such conditions are not required because sulfide mineralization formed below the sediment-water interface rather than within the water ambient column.

This contribution is the first detailed study of apatite from the HPD and investigates the REE-Y compositions of apatite in Zn-Pb mineralized and unmineralized phosphatic mudstone. The objectives of this study were to elucidate the relative timing of apatite formation and the ambient paleoredox conditions under which apatite precipitated. We also assess the origin of apatite and its relationship with SEDEX Zn-Pb deposit formation in the HPD.

Background

Geology of the HPD

The HPD is located within the eastern part of the Selwyn basin in the northern Canadian Cordillera. This basin was a passive continental margin setting in which thick sequences of Neoproterozoic to Lower Devonian sequences of fine-grained siliciclastic rocks with calcareous intercalations were deposited (Fig. 1A; Abbott et al., 1986; Gordey and Anderson, 1993). The HPD is flanked to the east by coeval carbonate rocks of the Mackenzie platform, whereas basinal strata extend to the west (Fig. 1A).

Paleogeographically, the Selwyn basin and Mackenzie platform were deposited on the west coast of the Laurentian continental margin near the equator (Cecile et al., 1997).

The HPD is hosted within the Duo Lake Formation. These sedimentary rocks are carbonaceous and calcareous to siliceous mudstones. Locally, the Duo Lake Formation is subdivided into informal members (Fig. 2A; Morganti, 1979) that, from the base to the top, comprise the Pyritic, Siliceous mudstone (PSMS), Lower Cherty mudstone (LCMS), Calcareous, Carbonaceous mudstone (CCMS), Active member (ACTM) and Upper Siliceous mudstone (USMS) (Morganti, 1979). The Steel Formation conformably overlies the Duo Lake Formation and is informally named the Flaggy mudstone (FLMD) (Morganti, 1979). Zinc-Pb SEDEX deposits, for which the HPD is renowned, are hosted within the ACTM. Conodont and graptolite biostratigraphic determinations show that deposition of the CCMS began in Middle Ordovician, was succeeded by the ACTM in the Early Silurian; this was, in turn, succeeded by the USMS in the Late Early to Middle Silurian (Norford and Orchard, 1985). Collectively, these sedimentary rocks comprise a semi-continuous, 38 km-long, southeast-to-northwest trend that defines the HPD (Fig. 1B).

The PSMS member (2 to 10 m thick) is the basal unit of the Duo Lake formation in the HPD and consists of grey to black pyritic, carbonaceous shale. The CCMS (50 to 100 m thick) overlies the PSMS member and consists of highly carbonaceous mudstones with variable amounts of intercalated limestone and carbonate concretions. Minor wispy pyrite and calcite veins, 2.5 mm to 1 cm, occur locally. The LCMS (15 to 30 m thick) consists of highly carbonaceous and siliceous mudstones. The CCMS and LCMS have very similar appearances and are massive and monotonous, highly carbonaceous cherty

mudstones with variable contents of calcite. These similarities hinder differentiation in the field, and both the LCMS and CCMS are typically logged as the CCMS. The ACTM (0 to 60 m thick; typically 20 to 30 m) hosts the Zn-Pb mineralization in the HPD. The USMS (20 to 90 m thick) consists of carbonaceous and cherty mudstones with minor to abundant laminations (0.5 to 1.5 cm thick) of apatite and locally abundant carbonate concretions. The carbonate concretions are spheroidal and range from a few centimeters to almost one meter in diameter. They are most abundant within the USMS, and are common in the CCMS and ACTM. Calcite is the predominant mineral, but a veneer of pyrite commonly rims the concretions.

Thinly bedded (0.5 to 1.5 cm thick) phosphorites occur within the upper CCMS, the lower ACTM and throughout the USMS (Goodfellow, 1984; Goodfellow and Jonasson, 1986). Within these beds, the dominant phosphate mineral is carbonate-bearing fluorapatite (herein referred to as apatite; Gadd et al., unpublished data). It is most commonly layered and is interlaminated with carbonaceous mudstone, chert and pyrite (Fig. 2B). Where phosphorites are present in the upper CCMS and lower ACTM, bulk-rock P_2O_5 contents range up to 10 wt.% over narrow (<0.5 m) stratigraphic intervals; however, the highest P_2O_5 abundances occur within the USMS. There, the P_2O_5 content commonly exceeds 10 wt.% over small (<1 m) intervals and averages ca. 5 wt.% over tens of meters (Goodfellow, 1984; Slack et al., 2011; Peter et al. in prep).

Methods

Sampling

The samples used in this current study are a subset of those for which LA-ICP-MS analyses of pyrite were reported (Gadd et al., 2015b). Included are five recent (2007-2011) diamond drill cores from the XY Central, Brodel and Don deposits (Fig. 1B). Polished petrographic sections of 10 representative phosphatic samples were analyzed from the CCMS (n=1), ACTM (n=2) and USMS (n=7). Among these samples, five were selected for electron probe microanalysis (EPMA) and all were analyzed by laser ablation-inductively coupled plasma-mass spectrometry (LA-ICP-MS).

Whole-rock geochemical analysis

Drill core samples collected from the XY Central, Don and Brodel deposits were analyzed at Acme Analytical Laboratories in Vancouver, British Columbia. Rock samples were crushed and pulverized using alumina-ceramic, and 5-g splits were decomposed using lithium borate. ICP-MS analyses were performed to measure the REE-Y abundances. Replicate data on in-house standards and duplicate samples indicate an acceptable reproducibility (within 15%) for the elements analyzed.

Electron probe microanalysis

EPMA analyses were performed using a JEOL JXA-8230 Superprobe® at Queen's University Facility for Isotope Research (QFIR), Kingston, Ontario. Prior to EPMA analyses, polished thin sections were carbon-coated to a standard thickness of 25 nm. Spot analyses were done using a beam diameter of 5-7 μm, a beam current of 15 nA and an accelerating potential of 15 kV. Peak and background counting times were 10 seconds for Ca and F, 20 seconds for P, 20 seconds for (proceeding elements not reported herein) Na, Si, Cl, S and Y and 40 seconds for Mg and Sr. Atomic number and absorption corrections were performed using the "PAP" corrections of Pouchou and Pichoir (1991),

and the characteristic fluorescence correction used is that of Reed (1990). The following standards, X-ray lines and crystals were used: synthetic magnesium fluoride, FKα, TAP; synthetic calcium pyrophosphate, CaKα, PET; synthetic calcium pyrophosphate, PKα, PET; albite, NaKα, TAP; synthetic diopside, MgKα, TAP; synthetic diopside, SiKα, TAP; scapolite, ClKα, PETH; anhydrite, SKα, PETH; strontianite, SrLα, PETH; synthetic yttrium phosphate, YLα, PETH.

Laser ablation-inductively coupled plasma-mass spectrometry

Laser ablation-ICP-MS analyses were carried out on a ThermoScientific Element XR® high resolution-ICP-MS coupled to a ESI NWR 193 nm ArF Excimer laser system equipped with a fast-washout large-format cell at Queen's University Facility for Isotope Research. Ablation was performed in an ultra-high purity He carrier gas. The HR-ICP-MS lens and gas flow settings were tuned daily on ^{238}U GSD-1G, a fused glass synthetic standard reference material (SRM) with 41 ppm U (Jochum et al. 2005), to maximize sensitivity (routinely >10^6 counts per second) and minimize oxides.

Isotopes (^{88}Sr, ^{89}Y, ^{137}Ba, ^{139}La, ^{140}Ce, ^{141}Pr, ^{146}Nd, ^{147}Sm, ^{153}Eu, ^{157}Gd, ^{159}Tb, ^{163}Dy, ^{165}Ho, ^{167}Er, ^{169}Tm, ^{172}Yb and ^{175}Lu) were analyzed at the medium nominal resolution setting (MR = 4000, where Resolution = M(center mass)/ΔM(peak width at 5% peak height)). Because isobaric interferences of Ba oxides overlap with Eu and because light REE and middle REE oxides overlap with middle REE and heavy REE, respectively, oxide production levels, measured as ^{238}U^{16}O/^{238}U, were maintained at <0.5%. This nominal mass resolution ensures that isobaric oxide interferences are avoided while maintaining high (sub-ppm) sensitivity during LA-ICP-MS analyses.

Analyses were performed using a beam diameter of 35 μm, with a laser pulse frequency of three hertz and a beam fluence of 10 J/cm^2. For each spot, 66 seconds of background (i.e., beam off) preceded 66 seconds of continuous ablation and each spot analysis consisted of ten 6.6-second scans. The laser bored through the thin section before 66 seconds in some analyses, in which case the data were integrated using fewer than 10 runs. This resulted in less integration time, but ensured more robust counting statistics. A three-point calibration curve was made from an analytical gas blank and standard reference materials GSD-1G (ca. 39 to 52 ppm REE-Y) and GSE-1G (ca. 390 to 600 ppm REE-Y) (Jochum et al., 2005) prior to each batch of unknown apatite analyses (≤10 spots) as external calibration standards. This was done to quantify elemental abundances in unknown apatite analyses and to correct for analytical drift. Additionally, an in-house matrix matched standard, Durango fluorapatite (Cerro de Mercado, Mexico), was measured subsequent to SRM analyses as an unknown to correct for differences in ablation yield; the unknown apatite data were corrected by Ce normalization using the Ce content of Durango apatite (4680 ppm), determined by EPMA. Data for unknowns and standards were acquired during the same analytical session using identical analytical protocols.

Durango apatite was also used to monitor precision and accuracy. Reproducibility of repeat analyses (n=10) across analytical sessions is better than 90% for all elements except Tm (87.6%), Yb (85.9%) and Lu (81.3%). Published REE-Y abundances for Durango apatite vary by a factor of 1.5 to 2 (Simonetti et al., 2008; Trotter and Eggins, 2006). The REE-Y content of Durango apatite determined in the current study falls

within the published range of REE-Y abundances, but are most consistent (i.e., within 25%) with data published by Trotter and Eggins (2006).

Measured REE-Y abundances were normalized against North American Shale Composite (NASC; Gromet et al., 1984). NASC-normalized values are marked with subscript "N". Anomalies are quantified ratios of measured and calculated values of a given element, and "*" denotes theoretical values calculated using the geometric mean of the neighboring elements following the convention of McLennan (1989): $Ce/Ce^* = Ce_N/(La_N * Pr_N)^{0.5}$, $Pr/Pr^* = Pr_N/(Ce_N * Nd_N)^{0.5}$, $Eu/Eu^* = Eu_N/(Sm_N^{0.67} * Tb_N^{0.33})$ $Gd/Gd^* = Gd_N/(Sm_N^{0.33} * Tb_N^{0.67})$ and $Y/Y^* = Y_N/(Dy_N * Ho_N)^{0.5}$. Note that Eu and Gd anomalies were calculated using the immediately adjacent elements to avoid overlapping anomalous behavior of Eu on Gd and of Gd on Eu.

Results

Petrography

Apatite in the studied samples is readily identified macroscopically as it forms well-defined, albeit thin (0.5 to 1.5 cm thick), beds (Fig. 2B). However, finer detail cannot be observed with standard petrographic microscopy because of the carbonaceous nature of the host rocks and the presence of minute detrital inclusions of quartz and organic matter within them. Therefore, scanning electron microscopy backscattered electron (BSE) imaging of apatite was done and this indicates the presence of predominantly bedded microcrystalline apatite aggregates (Fig. 3A-D). Apatite beds are parallel to, and interbedded with, carbonaceous mudstone (Figs. 2B, 3A-B). Apatite constitutes 50-90 vol.% within individual layers, and the remainder consists of variable

amounts of interstitial quartz, calcite, organic carbon and pyrite. Individual crystals within beds are minute (<10 μm), with forms that range from anhedral to subhedral. Coarser (50 to 100 μm) anhedral apatite partially replaces organic cell walls of microfossils (Fig. 3B, D, E, F). These microfossils are similar to acanthomorphic acritarchs (Kremer, 2005; Xiao et al., 2014), but in the HPD have previously been described as mazuelloids (Aldridge and Armstrong, 1981; Goodfellow and Jonasson, 1986; Norford and Orchard, 1985). Discrete apatite nodules are relatively uncommon within the carbonaceous mudstone matrix; however, micronodules (100 to 200 μm diameter) within apatite beds are fairly common and occur together with phosphatized microfossils and microcrystalline apatite (Fig. 3E). Apatite textures are consistent among the different stratigraphic units, regardless of whether this mineral is in the Zn-Pb mineralized ACTM or unmineralized CCMS and USMS.

Apatite major element and REE-Y compositions

The major element compositions of fluorapatite from the ACTM and USMS were measured by EPMA (Appendix 1). Average CaO/P_2O_5 ratios (1.332 to 1.369) and F/P_2O_5 ratios (0.094 to 0.107) indicate that the apatite composition falls between the end-members fluorapatite (CaO/P_2O_5 = 1.318; F/P_2O_5 = 0.089) and francolite (CaO/P_2O_5 = 1.621; F/P_2O_5 = 0.148). These ratios indicate that this phosphate mineral is carbonate-bearing fluorapatite, but the precise chemical formula of this apatite is difficult to determine by EPMA. Beam-induced F migration is a common problem in apatite and is controlled predominantly by crystal orientation (Pyle et al., 2002; Stock et al., 2015; Stormer et al., 1993). Ideally, the c-axis of apatite crystals should be oriented perpendicular to the electron beam to mitigate beam-induced F migration; however, the

minute grain size coupled with the random apatite crystal orientation in rock samples from the HPD did not permit such analyses. For these reasons, the measured F contents should be considered to be semi-quantative in nature.

Rare earth element-Y abundances were measured in apatite from the CCMS (*n*=9), ACTM (*n*=14) and USMS (*n*=60) (Appendix 2). Topologically, the NASC-normalized REE profiles for apatite are remarkably similar for each sample, regardless of its stratigraphic position (Fig. 4A). The total REE abundance varies among the different samples and is likely due to dilution by minute (<10 μm) clastic mineral grains interstitial to apatite microcrystals. All samples have moderately negative Ce/Ce* anomalies (0.46 to 0.76), positive Pr/Pr* anomalies (1.06 to 1.62) and positive Y/Y* anomalies (1.33 to 2.17). Eu/Eu* anomalies are predominantly weakly negative to weakly positive (0.81 to 1.62), with no apparent marked differences between apatites from mineralized and unmineralized strata (Fig. 4A). Gd/Gd* anomalies are weakly negative to moderately positive (0.79 to 1.96). Overall, these profiles are consistently flat with respect to NASC (Fig. 4A). One sample, XYC-224-184.0 from the ACTM, is somewhat enriched in middle rare earth elements (MREE) compared with the LREE and HREE. The relative degrees of LREE and MREE enrichment can be assessed quantitatively by calculating $(La/Sm)_N$ and $(La/Yb)_N$, respectively (Fig. 5). These data indicate minor LREE enrichment compared with HREE, and also indicate minimal MREE enrichment compared with LREE and HREE.

It is important to note that although much care was taken to analyze pure apatite during LA-ICP-MS analyses, the very fine-grained nature of this mineral in the HPD coupled with the abundant minute grains interstitial to microcrystalline apatite resulted in

inevitable ablation of some non-apatite minerals. The nearly identical topology of LA-ICP-MS apatite and lithogeochemical REE profiles (Fig. 4B) indicate that minute inclusions did not substantially influence the REE analyses determined by LA-ICP-MS.

Discussion

Stratigraphic distribution of apatite and variation in REE patterns

Bedded apatite spans three informal units within the HPD, the CCMS, ACTM and USMS, where it is interbedded with carbonaceous mudstone. The apatite is heterogeneously distributed, however, and the mineral is far more abundant in the USMS than in the CCMS and ACTM. Apatite textures vary little with respect to stratigraphic position, despite the occurrence of some apatite together with sphalerite- and galena-rich rocks of the ACTM. Apatite coexisting with sphalerite and galena is relatively uncommon, and the paragenetic relationship between apatite and base-metal sulfides is unclear. This is because sphalerite and galena textures experienced significant post-depositional modification (Gadd et al., 2015b; Jonasson and Goodfellow, 1986) and because crosscutting and/or overgrowth relationships among apatite, sphalerite and galena were not observed.

Apatite within the HPD is generally restricted to thin beds of minute, aggregated apatite crystals within the phosphorite-bearing units. It is widely recognized that phosphorites form during authigenesis and that apatite precipitates either on the seafloor or within the shallow subsurface near the sediment-water interface (Föllmi, 1996; Föllmi et al., 2005; Hein et al., 1993). The bedded nature of phosphorites is typically attributed to slow sedimentation and mechanical reworking of the sediments (Föllmi, 1996; Föllmi

et al., 2005; Glenn et al., 1994). The former physical process prevents dilution by clastic material, whereas the latter concentrates apatite into nearly monomineralic beds. Phosphatic mudstone within the HPD resembles phosphorite-bearing carbonaceous mudstones from other localities (e.g., Miocene Monterey Bay Formation; Föllmi et al., 2005), suggesting that similar physico-chemical processes were responsible for phosphogenesis in the HPD (see below).

Ubiquitous phosphatic microfossils within apatite-rich beds (Fig. 3D-F) have previously been described as mazuelloids in the HPD (Norford and Orchard, 1985), and were considered planktonic microorganisms with phosphatic cell walls that proliferated in response to hydrothermal fluid discharge (Goodfellow and Jonasson, 1986). Since then, it has been recognized that mazuelloids are acanthomorphic acritarch microfossils, and that phosphatization is largely a postmortem process (Kremer, 2005; Kremer, 2011). This reinterpretation indicates that apatite deposition commenced postmortem and persisted into early diagenesis; furthermore, the abundance of acanthomorphic acritarch microfossils is indicative of large upwelling-derived algal blooms (Kremer, 2005; Kremer, 2011).

Apatite in the HPD is an important repository for REE-Y, as indicated by a strong positive correlation between bulk-rock P_2O_5 and ΣREE (not shown). The topology of the NASC-normalized REE-Y patterns for apatite within the CCMS, ACTM and USMS are remarkably consistent and there is no systematic variability among the apatite samples with stratigraphic position. The total REE abundances vary somewhat among the samples, and this is likely related to the presence of minute detrital grains that are spatially unresolvable using the transient LA-ICP-MS signal. It is important to determine

the relative role possible contaminants, as these may skew the topology of the REE profiles. In Figure 4B, bulk phosphatic mudstone REE profiles from the HPD are compared with those for apatite, as determined by LA-ICP-MS. It is clear from this comparison that: 1) the bulk rock and LA-ICP-MS data are topologically similar; 2) the primary difference between the REE profiles is the overall REE (i.e., up and down shift) abundances; and 3) the REE abundances are predominantly controlled by REE adsorption/substitution mechanisms onto/into apatite within the phosphatic mudstone at the HPD.

The incorporation of trivalent REE-Y into divalent Ca sites within the apatite crystal lattice implies that a coupled substitution must occur in order to maintain charge balance. Rønsbo (1989) and Hughes et al. (1991) demonstrated that charge balance in apatite for REE-Y substitution is achieved by $Na^{+} + REE^{3+} = 2Ca^{2+}$ and/or by $Si^{4+} + REE^{3+} = Ca^{2+} + P^{5+}$ coupled substitutions. It is not possible, however, to assess the predominant substitution mechanism for apatite from the HPD because Na and REE-Y are typically below EPMA detection limits and the Si content is variable (Appendix 1). Mineral phases other than apatite (e.g., clay minerals) likely contain some REE, but the close correspondence between LA-ICP-MS and lithogeochemical data (Fig. 4B) indicate that apatite is the predominant control on the NASC-normalized REE distributions for phosphatic mudstones within the HPD.

Preservation of seawater REE signature

The topology of the shale-normalized REE profiles in authigenic and biogenic phosphates is commonly invoked as a proxy for REE behavior in seawater (Emsbo et al.,

2015; Garnit et al., 2012; Joosu et al., 2015; Wright et al., 1987). In order for this to be valid, the relative timing of phosphogenesis must be synsedimentary (i.e., authigenic) and not late diagenetic, as signatures can have been modified (Lécuyer et al., 2004; Reynard et al., 1999). Reynard et al. (1999) proposed that REE profiles of apatite may reflect quantitative uptake of hydrogenous (i.e., derived from ambient seawater) REE or that adsorption and substitution processes modify primary REE profiles subsequent to deposition. Quantitative uptake results in no fractionation amongst the REE, and such apatite should possess seawater-like NASC-normalized REE profiles. The adsorption mechanism is governed by surficial crystal-chemical properties, whereby LREE are preferentially adsorbed onto apatite crystal surfaces over the HREE, and this occurs predominantly during early diagenesis (Lécuyer et al., 2004; Reynard et al., 1999). The substitution mechanism, however, is controlled by REE substitution into the apatite crystal lattice. Apatites affected by substitution significantly incorporate MREE over LREE and HREE due to the similar ionic radii of MREE and Ca, and this results in concave-down NASC-normalized REE profiles (Fig. 4B); this process is indicative of recrystallization during late diagenesis or deeper burial (Lécuyer et al., 2004; Reynard et al., 1999; Shields and Stille, 2001).

Both adsorption and substitution mechanisms can be assessed quantitatively by calculating $(La/Yb)_N$ and $(La/Sm)_N$ NASC-normalized ratios (Fig. 5). $(La/Yb)_N$ values >1 reflect a greater degree of LREE enrichment with respect to HREE because LREE are adsorbed onto apatite crystal surfaces; however, Reynard et al. (1999) suggest that values below 2.5 are indicative only of minor adsorption during early diagenesis. The average values for apatite from the HPD range from 1.32 to 2.74, suggesting that early diagenetic

fluids did not significantly modify primary LREE/HREE distributions. Similarly, $(La/Sm)_N$ ratios reveal fractionation characteristics of LREE to MREE. Lécuyer et al. (2004) suggest that values >0.3 are most likely primary or only slightly altered, whereas values <0.3 have significant MREE addition (via substitution) within the crystal structure. Average $(La/Sm)_N$ ratios of apatites from the HPD range from 0.47 to 1.38. One sample from the ACTM, XYC-224-184.0, has lower $(La/Sm)_N$ ratios that form a separate cluster (Fig. 5). This sample is interbedded with sphalerite and galena, but the paragenetic relationship between apatite and base-metal sulfides is unclear (see above). Gadd et al. (2015b) proposed that the introduction of sphalerite and galena SEDEX mineralization is largely early diagenetic. If apatite deposition predated SEDEX mineralization, then SEDEX Zn-Pb fluids may have modified the original REE content; however, these lower $(La/Sm)_N$ values are above the minimum threshold for significant MREE substitution proposed by Lécuyer et al. (2004). Thus, according to the diagenetic alteration proxies of Reynard et al. (1999) and Lécuyer et al. (2004), the REE contents of apatite from the HPD were not significantly modified by early or late diagenetic fluids. As such, it is likely that the REE contents apatite serve as a reliable proxy of the REE systematics of the ambient fluid in it was deposited.

REE as redox proxies: Ce/Ce* and Eu/Eu*

Cerium and Eu are the only REE that deviate from the (III) valence state. Cerium has two oxidation states, Ce^{3+} and Ce^{4+}, and these are strongly redox dependent; fractionation of Ce relative to its neighboring elements is a direct response to the variability in oxidation state (De Baar et al., 1988). In oxygenated marine environments, Ce^{4+} predominates and is scavenged by highly reactive Fe-Mn-oxyhydroxides, which

leads to depletion of Ce in oxic seawater (Elderfield and Greaves, 1982). In modern oceanic environments, the magnitude of the Ce anomaly is dependent on water depth. In surface waters, Ce anomalies are largely absent (Ce/Ce* ~1); however, Ce becomes depleted in seawater at progressively greater depths due to oxidative scavenging onto highly reactive Fe-Mn-oxyhydroxides particles in the water column (Alibo and Nozaki, 1999). Whereas Fe-Mn-oxyhydroxide particles gain Ce^{4+} and possess positive Ce anomalies, authigenic phases that precipitate from Ce-depleted seawater near the sediment-water interface, such as apatite, are also depleted in Ce and display negative Ce anomalies (i.e., Ce/Ce*<1). In anoxic environments, Ce behaves similarly to the other trivalent REE, and nil to weakly positive anomalies are present. Thus, depending on ambient redox and reactive particle residence time, apatite may record negative, positive or nil Ce anomalies.

The magnitude of negative Ce anomalies is commonly used as a proxy to infer the oxygen levels under which authigenic minerals, such as apatite, are deposited (Wright et al., 1987). Apatite from sedimentary phosphorites commonly displays strongly negative to nil Ce anomalies (see recent compilation by Emsbo et al., 2015). Apatite deposited under oxic conditions (i.e., >2 ml O_2/L H_2O; Tribovillard et al., 2006) has the lowest Ce anomalies (Ce/Ce*<0.4) owing to the significant fractionation of Ce by oxidative scavenging. Moderately negative Ce anomalies (Ce/Ce*=0.4 to 0.9), however, are the byproduct of suboxic conditions (i.e., 0.2 to 2 ml O_2/L H_2O; Tribovillard et al., 2006) because a portion of the Ce is released into bottom waters or sediment porewaters during reductive dissolution of particulate material onto which Ce oxides absorbed (Elderfield and Sholkovitz, 1987; Haley et al., 2004; Wright et al., 1987).

It is important to determine whether a calculated Ce/Ce* records truly deficient (Fig. 6, Field IIIb) or excess (Fig. 6, Field IIIa) Ce relative to the neighboring lanthanides, or whether the Ce/Ce* is related to deficient (Fig. 6, Field IIb) or excess (Fig. 6, Field IIa) abundances of La, resulting in the generation of false or spurious Ce anomalies (Bau and Dulski, 1996). This can be done by calculation of Pr/Pr* ratios, because negative Ce/Ce* (<1.0) results *a priori* in positive Pr/Pr* (>1.0). The LA-ICP-MS data for apatite plot entirely within Field IIIb on the Ce/Ce* vs. Pr/Pr* scatterplot (Fig. 6) used to discriminate between genuine and spurious anomalies (Bau and Dulski, 1996). These data therefore indicate true negative Ce anomalies that are unrelated to La/La*. Importantly, the negative Ce anomalies constrain the ambient redox conditions to suboxic during apatite deposition (Wright et al., 1987). As these are all of nearly identical magnitude, it is likely that suboxic conditions persisted during apatite formation in the HPD. Due to the effects of REE mobilization during diagenesis, the veracity of Ce anomalies in apatite as a paleoredox indicator has been the subject of much scrutiny and considerable debate (Shields and Stille, 2001 and references therein). Thus, the REE composition of apatite may reflect the composition of deeper porewaters and not ambient bottom water conditions. However, our data demonstrate minimal post-depositional modification (Fig. 5) and retention of primary REE signatures.

The relative abundance of the two oxidation states of Eu, Eu^{2+} and Eu^{3+}, is controlled by redox, pH and temperature. At low temperature (ca. 25 °C) near surface conditions, Eu prevails in its trivalent state (Sverjensky, 1984). Accordingly, Eu^{3+} will not fractionate relative to its neighboring trivalent elements, and no anomaly is produced. However, Eu^{2+} dominates under extremely reducing (i.e., anoxic) alkaline conditions or

high temperature (i.e., >250 °C) hydrothermal conditions and will fractionate relative to the adjacent REE (Sverjensky, 1984). Thus, depending on the redox, pH and temperature conditions of deposition, apatite may record positive, nil or negative Eu anomalies.

Igneous apatite commonly displays negative Eu anomalies (e.g., Durango fluorapatite; Fig. 4C) (Belousova et al., 2002), whereas phosphorite apatite commonly records either nil or minimally positive Eu anomalies (Fig. 4A-C) (Emsbo et al., 2015; Joosu et al., 2015; Shields and Stille, 2001). Strongly positive Eu anomalies (Eu/Eu*>>1) are comparatively rare, but have been documented in apatite deposited from high temperature (>250 °C) hydrothermal deposits (Fig. 4C), such as the Heath Steele belt iron formation (Eu/Eu* = 25.3; Peter et al., 2003) and the Panasquiera hydrothermal tin deposit (Eu/Eu* = 35.6; Knutson et al., 1985). The inferred hydrothermal Zn-Pb SEDEX fluid temperatures for the HPD, estimated using sphalerite-galena S isotope thermometry, are low (i.e., <200 °C; Goodfellow and Jonasson, 1986). These low temperature fluids likely precluded the fractionation of Eu in the Eu^{2+} state and the formation of (positive) Eu anomalies. The relatively unfractionated behavior of NASC-normalized Eu in apatite from the HPD (Fig. 4A, B) indicates that Eu predominated in its trivalent state, and that Eu was neither enriched nor depleted relative to the other REE. Because the lack of a strong positive (or negative) Eu anomaly in apatite may be the result of several combined physico-chemical factors (e.g., limited water-rock interaction, fluid temperature, pH, redox conditions; Douville et al., 1999; Michard, 1989), these data alone cannot be used to differentiate between apatite deposition from low temperature hydrothermal fluids and that formed by hydrogenous processes.

Gd behavior

Gadolinium is trivalent and possesses similar chemical properties to the REE; however, anomalous Gd behavior, relative to neighboring Eu and Tb, has been documented in modern seawater (De Baar et al., 1985). The documented Gd anomalies are weakly positive (Gd/Gd* = 1.1-2), and are relatively constant with respect to water depth (De Baar et al., 1985). The fractionation of Gd relative to Eu and Tb is not a redox related process because Gd is exclusively trivalent. Therefore, Gd anomalies must form in response to some other intrinsic property of Gd. The most likely explanation is the relatively stable electron configuration of Gd, in which half of the outer 4f electron shell is filled (i.e., tetrad effect; Bau, 1999). Bau (1999) investigated mechanisms by which dissolved REE-Y are scavenged onto precipitating Fe oxyhydroxides. The experimental data of Bau (1999) reveal that scavenging is pH dependent and that tetrad REE-Y (Y, La, Gd and Lu) remain in solution relative to non-tetrad REE at pH>5; in low pH fluids, tetrad REE-Y do not fractionate relative to Eu and Tb. Kim et al. (1991) demonstrated that a fluid may possess positive or negative Gd anomalies. The predominant factor controlling anomalous Gd behavior is alkalinity and carbonate complexation; however, the higher particle reactivity of neighboring Eu and Tb also factor into the generation of Gd anomalies (Kim et al., 1991). Solutions with weakly acid to near neutral pH typically possess positive Gd anomalies, whereas alkaline solutions possess negative Gd anomalies. The Gd/Gd* values of apatite from the HPD are relatively constant (Fig. 4A-B), with average values ranging from 1.11 to 1.36 (Appendix 2). Late Ordovician and Early Silurian phosphorites of Emsbo et al. (2015) also show positive Gd/Gd* values (Fig. 4B). In fact, a majority of the Phanerozoic phosphorite REE data presented in Emsbo et al. (2015) possess positive Gd anomalies that are of similar magnitude (Fig. 3

in Emsbo et al., 2015). Although once considered controversial due to potential analytical artifacts and shale normalization schemes, Alibo and Nozaki (1999) demonstrated that Gd anomalies in seawater are genuine and suggested that anomalous Gd behavior in seawater may be controlled by kinetic mechanisms of ocean circulation and biogeochemical nutrient cycling. The Gd anomalies in apatite from the HPD are also genuine because oxide production was minimized to avoid the isobaric LREE-oxide interferences (e.g., $^{16}O^{141}Pr$ on ^{157}Gd) that are responsible for spurious Gd anomalies (Dulski, 1994). Additionally, Gd anomalies are observed in both LA-ICP-MS and lithogeochemical REE profiles (Fig. 4B). Gadolinium anomalies in apatite are not typically discussed in the REE-Y literature; however, these anomalies in apatite from the HPD suggest that seawater mediated the precipitation of this mineral. Additional research is needed to more completely assess the utility of these anomalies, as they may potentially provide additional insight into the physico-chemical conditions (e.g., pH, alkalinity, temperature) under which apatite is deposited.

Y behavior

Yttrium is trivalent and possesses similar chemical properties to the REE. The element is considered a geochemical twin to Ho because these two elements have similar or identical ionic radii and valences, respectively (Bau et al., 1996). Whereas the continental crust, mantle and high temperature hydrothermal fluids are characterized by chondritic Y/Ho ratios (i.e., 26), seawater has super-chondritic Y/Ho ratios (ca. 47) (Bau, 1996; Nozaki et al., 1997). Y/Ho ratio variability between seawater and the other media is due to higher particle-reactivity of Ho, which is scavenged preferentially over Y by hydrogenous ferromanganese oxyhydroxide particles in the marine environment (Bau,

1996; Bau, 1999; Bau et al., 1996; Koschinsky et al., 1997). The Y/Ho ratio of apatite from the HPD is relatively constant, with average values ranging from 37.6 to 43.8 (Appendix 2). These values are consistent with the positive Y anomalies (1.53 to 1.87). Although it is unlikely that marine conditions were identical to those in the modern Pacific Ocean, the super-chondritic Y/Ho ratios and positive Y anomalies suggest a predominant seawater source for apatite within the HPD.

Origin of phosphatic mudstone

Marine phosphate deposits are common in continent marginal sediments, and formed particularly during several peak time intervals in the Phanerozoic (Cook and McElhinny, 1979). Phosphatic sediments occur in many different forms, some of which include irregular masses, granular beds and nodules (Glenn et al., 1994). These deposits can form by several processes, but the most commonly invoked is the upwelling of nutrient-rich waters (Cook and McElhinny, 1979; Föllmi, 1996; Föllmi et al., 2005; Froelich et al., 1988). It is also recognized that large sulfur (oxidizing) bacteria play an important role in releasing dissolved phosphate to sediment porewaters in modern upwelling environments (e.g., Namibian shelf; Schulz and Schulz, 2005).

Non-upwelling environments are also important sinks for marine P and include continental margins that lack seasonal upwelling (e.g., Long Island sound; Ruttenberg and Berner, 1993). Phosphate dissolved in seawater may also sorb onto hydrogenous Fe-Mn oxyhydroxide crusts, and subsequently form authigenic apatite during diagenesis (Bau et al., 1996; Koschinsky et al., 1997). Hydrothermal phosphogenesis has also been invoked, particularly in places where phosphatic and metalliferous sedimentary rocks

occur together (Goodfellow, 1984; Peter and Goodfellow, 1996; Peter et al., 2003; Stalder and Rozendaal, 2004); however, it is unclear in these ancient deposits whether the P is derived from hydrothermal fluids, together with other hydrothermal elements, or whether the P is hydrogenous and scavenged efficiently by hydrothermal Fe-Mn particles and released during diagenesis to form apatite. In modern seafloor hydrothermal vents, P is scavenged from seawater and adsorbed onto hydrothermal Fe-Mn-oxyhydroxide particles (Feely et al., 1990; Feely et al., 1998; Wheat et al., 1996).

One method to evaluate the processes responsible for phosphogenesis within the HPD is to compare the REE characteristics of apatite with those formed by different genetic processes. The HPD apatite are most similar in their REE compositions to sedimentary phosphorite (Fig. 4B), and are dissimilar to low temperature hydrothermal, high temperature hydrothermal or igneous apatites (Fig. 4C). Moreover, the topology of the apatite REE profiles for the HPD apatite is almost identical to Late Ordovician phosphorites from southeastern Missouri (Fig. 4B). Notably, however, the phosphorites from Missouri Lack a distinct negative Ce/Ce* (Emsbo et al., 2015). Although Goodfellow (1984) suggested that the close spatial association of phosphatic mudstone with Zn-Pb SEDEX deposits in the HPD is the consequence of a shared (common) hydrothermal origin, our REE data support a hydrogenous origin for the apatite. Such an origin is supported by the chemical uniformity (particularly the REE profiles) of the apatite from the different sedimentary units (Fig. 4A). Although one of the units (i.e., ACTM) hosts the Zn-Pb deposits, the striking similarity of the REE profiles for the mineralized and unmineralized rocks indicates that the apatite has a common origin that is unrelated to the venting of hydrothermal fluids, but rather is due to precipitation from

ambient bottom water. Additional support for a seawater origin is the presence of age-equivalent phosphatic mudstones elsewhere in the Selwyn basin that lack associated Zn-Pb deposits (Goodfellow et al., 1992).

Implications

The REE contents of apatite from the HPD place unequivocal constraints on the ambient water column redox conditions. The Ce anomaly data for apatite in both mineralized and unmineralized rocks indicate that the redox state of the ambient bottom water was suboxic during apatite deposition. These include data for host rocks that are stratigraphically below and above mineralization that formed prior to, and subsequent to mineralization, respectively. The suboxic nature of the water column negates the presence of sulfidic conditions in the ambient water column purported to have existed over a sustained period of time (up to 50 M.y.), as suggested by Goodfellow (1987). These data do not preclude the occurrence of intermittent anoxic or sulfidic ambient conditions, but the intrinsic redox sensitivity of Ce and the preservation of negative Ce anomalies imply that the prevailing phosphogenic conditions were suboxic.

Our data strongly support a hydrogenous authigenic origin for apatite in the HPD. In the absence of low temperature hydrothermal phosphogenesis, it is probable that a sedimentary and/or biogeochemical process(es) mediated the deposition of phosphate. Slack et al. (2011) proposed that phosphogenesis was driven by the upwelling of nutrient-rich waters which were subsequently trapped to produce phosphatic mudstone at the HPD. The paleogeographic configuration of the western Laurentian continental margin, the presence of abundant upwelling-produced acritarch microfossils (Kremer, 2011),

similarities of the REE abundances with other time-equivalent phosphorites provide evidence for an upwelling origin. Alternatively, several workers have proposed that sustained stagnant conditions existed (Goodfellow, 1987; Johnson et al., 2014; Turner, 1992), and these conditions do not conform to traditional upwelling models. Therefore, although the apatite REE data from the HPD support a hydrogenous origin, additional research, such as independent redox proxies (Mo, Re, etc.), sedimentological data, paleo-water depth indicators and bacterial biomarkers, is needed to better understand phosphogenesis in the HPD.

The close spatial association of phosphatic mudstone and SEDEX Zn-Pb deposits might suggest a common hydrothermal origin; however, our data indicate that phosphogenesis in the HPD is only casually related to SEDEX Zn-Pb mineralization. Additional data for apatite from the HPD, such as stable S, C and O isotopes in structurally associated sulfate and carbonate, respectively, is required to better understand the ambient paleoenvironmental and/or later diagenetic conditions that led to the formation and preservation of the world-class Zn-Pb SEDEX deposits.

Acknowledgments

This research was jointly funded by NSERC-CRD 387591-09, CAMIRO Project 08E04 “Geochemistry of Shales as Vectors to Ore Deposits” and the Targeted Geoscience Initiative-4 Program of the Geological Survey of Canada. We thank Don Chipley and Brian Joy of Queen’s Facility for Isotope Research for their assistance with LA-ICP-MS and EPMA, respectively. We thank Jason Dunning, Gabe Xue, Wolfgang Schleiss and Jelle DeBruyckere of Selwyn Chihong Mining Ltd. for providing access to

drill core samples and technical information, without which this work could not have been completed. Insightful and thorough reviews by Hechmi Garnit, Simon Jackson and R. Chris Tacker greatly improved this manuscript. We sincerely thank the SEGCF for financial support. This is Geological Survey of Canada contribution 20150298.

References

Abbott, J.G., Gordey, S.P., and Tempelman-Kluit, D.J. (1986) Setting of stratiform, sediment-hosted lead-zinc deposits in Yukon and northeastern British Columbia. In J.A. Morin, Ed. Mineral Deposits of Northern Cordillera: Canadian Institute of Mining and Metallurgy, Special Volume 37, p. 1-18.

Aldridge, R.J., and Armstrong, H.A. (1981) Spherical phosphatic microfossils from the Silurian of North Greenland. Nature, 292, 531-533.

Alibo, D.S., and Nozaki, Y. (1999) Rare earth elements in seawater: Particle association, shale-normalization, and Ce oxidation. Geochimica et Cosmochimica Acta, 63(3-4), 363-372.

Arning, E.T., Birgel, D., Brunner, B., and Peckmann, J. (2009) Bacterial formation of phosphatic laminites off Peru. Geobiology, 7(3), 295-307.

Bau, M. (1996) Controls on the fractionation of isovalent trace elements in magmatic and aqueous systems: Evidence from Y/Ho, Zr/Hf, and lanthanide tetrad effect. Contributions to Mineralogy and Petrology, 123(3), 323-333.

-. (1999) Scavenging of dissolved yttrium and rare earths by precipitating iron oxyhydroxide: Experimental evidence for Ce oxidation, Y-Ho fractionation, and lanthanide tetrad effect. Geochimica et Cosmochimica Acta, 63(1), 67-77.

Bau, M., and Dulski, P. (1996) Distribution of yttrium and rare-earth elements in the Penge and Kuruman iron-formations, Transvaal Supergroup, South Africa. Precambrian Research, 79(1-2), 37-55.

Bau, M., Koschinsky, A., Dulski, P., and Hein, J.R. (1996) Comparison of the partitioning behaviours of yttrium, rare earth elements, and titanium between hydrogenetic marine ferromanganese crusts and seawater. Geochimica et Cosmochimica Acta, 60(10), 1709-1725.

Belousova, E.A., Griffin, W.L., Reilly, S.Y., and Fisher, N.I. (2002) Apatite as an indicator mineral for mineral exploration: trace-element compositions and their relationship to host rock type. Journal of Geochemical Exploration, 76(1), 45-69.

Cecile, M.P., Morrow, D.W., and Williams, G.K. (1997) Early Paleozoic (Cambrian to Early Devonian) tectonic framework, Canadian Cordillera. Bulletin of Canadian Petroleum Geology, 45(1), 54-74.

Cook, P.J., and McElhinny, M.W. (1979) A reevaluation of the spatial and temporal distribution of sedimentary phosphate deposits in the light of plate tectonics. Economic Geology, 74(2), 315-330.

De Baar, H.J.W., Brewer, P.G., and Bacon, M.P. (1985) Anomalies in rare-earth distributions in seawater: Gd and Tb. Geochimica et Cosmochimica Acta, 49(9), 1961-1969.

De Baar, H.J.W., German, C.R., Elderfield, H., and van Gaans, P. (1988) Rare-earth element distributions in anoxic waters of the Cariaco Trench. Geochimica et Cosmochimica Acta, 52(5), 1203-1219.

Douville, E., Bienvenu, P., Charlou, J.L., Donval, J.P., Fouquet, Y., Appriou, P., and Gamo, T. (1999) Yttrium and rare earth elements in fluids from various deep-sea hydrothermal systems. Geochimica et Cosmochimica Acta, 63(5), 627-643.

Dulski, P. (1994) Interferences of oxide, hydroxide and chloride analyte species in determination of rare earth elements in geological samples by inductively coupled plasma-mass spectrometry. Fresenius Journal of Analytical Chemistry, 350, 194-203.

Elderfield, H., and Greaves, M.J. (1982) The rare earth elements in seawater. Nature, 296, 214-218.

Elderfield, H., and Sholkovitz, E.R. (1987) Rare-earth elements in the pore waters of reducing nearshore sediments. Earth and Planetary Science Letters, 82(3-4), 280-288.

Emsbo, P., McLaughlin, P.I., Breit, G.N., Bray, E.A.d., and Koenig, A.E. (2015) Rare earth elements in sedimentary phosphate deposits: Solution to the global REE crisis? Gondwana Research, 27, 776-785.

Feely, R.A., Massoth, G.J., Baker, E.T., Cowen, J.P., Lamb, M.F., and Krogslund, K.A. (1990) The effect of hydrothermal processes on midwater phosphorus distributions in the northeast Pacific. Earth and Planetary Science Letters, 96(3-4), 305-318.

Feely, R.A., Trefry, J.H., Lebon, G.T., and German, C.R. (1998) The relationship between P/Fe and V/Fe ratios in hydrothermal precipitates and dissolved phosphate in seawater. Geophysical Research Letters, 25(13), 2253-2256.

Föllmi, K.B. (1996) The phosphorus cycle, phosphogenesis and marine phosphate-rich deposits. Earth-Science Reviews, 40(1-2), 55-124.

Föllmi, K.B., Badertscher, C., de Kaenel, E., Stille, P., John, C.M., Adatte, T., and Steinmann, P. (2005) Phosphogenesis and organic-carbon preservation in the Miocene Monterey Formation at Naples Beach, California—The Monterey hypothesis revisited. Geological Society of America Bulletin, 117(5), 589-619.

Froelich, P.N., Arthur, M.A., Burnett, W.C., Deakin, M., Hensley, V., Jahnke, R., Kaul, L., Kim, K.H., Roe, K., Soutar, A., and Vathakanon, C. (1988) Early diagenesis of organic-matter in Peru continental-margin sediments: Phosphorite precipitation. Marine Geology, 80(3-4), 309-343.

Gadd, M.G., Layton-Matthews, D., Peter, J.M., and Paradis, S. (2015a) In situ Trace Element and Sulphur Isotope Analyses of Pyrite Constrain Timing of Mineralization and Sources of Sulphur in the Howard's Pass SEDEX Zn-Pb District, Yukon. In S. Paradis, Ed. Targeted Geoscience Initiative 4: Sediment-hosted Zn-Pb deposits: Processes and implications for exploration, p. 58-74. Geological Survey of Canada, Open File 7838.

-. (2015b) The world-class Howard's Pass SEDEX Zn-Pb district, Selwyn Basin Yukon. Part I: Trace element compositions of pyrite record input of hydrothermal, diagenetic and metamorphic fluids to mineralization. Mineralium Deposita.

Garnit, H., Bouhlel, S., Barca, D., and Chtara, C. (2012) Application of LA-ICP-MS to sedimentary phosphatic particles from Tunisian phosphorite deposits: Insights from trace elements and REE into paleo-depositional environments. Chemie der Erde-Geochemistry, 72(2), 127-139.

Glenn, C.R., Follmi, K.B., Riggs, S.R., Baturin, G.N., Grimm, K.A., Trappe, J., Abed, A.M., Galliolivier, C., Garrison, R.E., Ilyin, A.V., Jehl, C., Rohrlich, V., Sadaqah, R.M.Y., Schidlowski, M., Sheldon, R.E., and Siegmund, H. (1994) Phosphorus and phosphorites: Sedimentology and environments of formation. Eclogae Geologicae Helvetiae, 87(3), 747-788.

Goodfellow, W.D. (1984) Geochemistry of rocks hosting the Howards Pass (XY) strata-bound Zn-Pb deposit, Selwyn basin, Yukon Territory, Canada. Proceedings of the Sixth Quadrennial IAGOD Symposium, 6, 91-112.

-. (1987) Anoxic stratified oceans as a source of sulphur in sediment-hosted stratiform Zn-Pb deposits (Selwyn Basin, Yukon, Canada). Chemical Geology: Isotope Geoscience Section, 65(3), 359-382.

-. (1999) Sediment-hosted Zn-Pb-Ag deposits of North America. In O. Holm, J. Pongratz, and P. McGoldrick, Eds. Basins, Fluids and Zn-Pb ores, p. 59-92. CODES Special Publication 2, Tasmania, Australia.

-. (2007) Base metal metallogeny of the Selwyn Basin, Canada. Mineral Resources of Canada: A Synthesis of Major Deposit-Types, District Metallogeny, the Evolution of Geological Provinces, and Exploration Methods: Geological Association of Canada, Mineral Deposits Division, Special Publication, 5, 553-579.

Goodfellow, W.D., and Jonasson, I. (1986) Environment of formation of the Howards Pass (XY) Zn-Pb deposit, Selwyn Basin, Yukon. In J.A. Morin, Ed. Mineral Deposits of Northern Cordillera: Canadian Institute of Mining and Metallurgy, Special Volume 37, p. 19-50.

Goodfellow, W.D., Nowlan, G.S., McCracken, A.D., Lenz, A.C., and Grégoire, D.C. (1992) Geochemical anomalies near the Ordovician□Silurian boundary, northern Yukon Territory, Canada. Historical Biology, 6(1), 1-23.

Gordey, S.P., and Anderson, R.G. (1993) Evolution of the northern Cordilleran miogeocline, Nahanni map area (105I), Yukon and Northwest Territories. 214 p. Geological Survey of Canada Memoir 428.

Gromet, L.P., Haskin, L.A., Korotev, R.L., and Dymek, R.F. (1984) The "North American shale composite": Its compilation, major and trace element characteristics. Geochimica et Cosmochimica Acta, 48(12), 2469-2482.

Haley, B.A., Klinkhammer, G.P., and McManus, J. (2004) Rare earth elements in pore waters of marine sediments. Geochimica et Cosmochimica Acta, 68(6), 1265-1279.

Hein, J.R., Yeh, H.-W., Gunn, S.H., Sliter, W.V., Benninger, M., and Wang, C.-H. (1993) Two major Cenozoic episodes of phosphogenesis recorded in equatorial Pacific seamount deposits. Paleoceanography, 8(2), 293-311.

Hughes, J.M., Cameron, M., and Mariano, A.N. (1991) Rare-Earth-Element Ordering and Structural Variations in Natural Rare-Earth-Bearing Apatites. American Mineralogist, 76(7-8), 1165-1173.

Jochum, K.P., Willbold, M., Raczek, I., Stoll, B., and Herwig, K. (2005) Chemical characterisation of the USGS reference glasses GSA-1G, GSC-1G, GSD-1G, GSE-1G, BCR-2G, BHVO-2G and BIR-1G Using EPMA, ID-TIMS, ID-ICP-MS and LA-ICP-MS. Geostandards and Geoanalytical Research, 29(3), 285-302.

Johnson, C.A., Slack, J., Falck, H., and Kelley, K.D. (2014) Depositional environment of mudstone host rocks at the Howards Pass Zn-Pb deposits, Yukon Territory, Canada: Insights from iron speciation, sulfur isotopes, and bulk Fe/Al And Mo/TOC Ratios. Geological Society of America Abstracts with Programs, 46, 794.

Jonasson, I.R., and Goodfellow, W.D. (1986) Sedimentary and diagenetic textures, and deformation structures within the sulphide zone of the Howards Pass (XY) Zn-Pb deposit, Yukon and Northwest Territories. In J.A. Morin, Ed. Mineral Deposits of Northern Cordillera: Canadian Institute of Mining and Metallurgy, Special Volume 37, p. 51-70.

Joosu, L., Lepland, A., Kirsimäe, K., Romashkin, A.E., Roberts, N.W., Martin, A.P., and Črne, A.E. (2015) The REE-composition and petrography of apatite in 2 Ga Zaonega Formation, Russia: The environmental setting for phosphogenesis. Chemical Geology, 395, 88-107.

Kim, K.H., Byrne, R.H., and Lee, J.H. (1991) Gadolinium behavior in seawater: A molecular-basis for gadolinium anomalies. Marine Chemistry, 36(1-4), 107-120.

Kirkham, G., Dunning, J., and Schleiss, W. (2012) Update for Don deposit mineral resource estimate, Howard's Pass property, eastern Yukon, Selwyn Resources Ltd., NI 43-101 Technical Report, p. 145.

Knutson, C., Peacor, D.R., and Kelly, W.C. (1985) Luminescence, color and fission-track zoning in apatite crystals of the Panasqueira tin-tungsten deposit, Beira-Baixa, Portugal. American Mineralogist, 70(7-8), 829-837.

Koschinsky, A., Stascheit, A., Bau, M., and Halbach, P. (1997) Effects of phosphatization on the geochemical and mineralogical composition of marine ferromanganese crusts. Geochimica et Cosmochimica Acta, 61(19), 4079-4094.

Kremer, B. (2005) Mazuelloids: product of post-mortem phosphatization of acanthomorphic acritarchs. Palaios, 20(1), 27-36.

Kremer, B. (2011) High productivity of Early Silurian sea evidenced by post-bloom macroaggregates. Sedimentary Geology, 240(3-4), 115-122.

Lécuyer, C., Reynard, B., and Grandjean, P. (2004) Rare earth element evolution of Phanerozoic seawater recorded in biogenic apatites. Chemical Geology, 204(1-2), 63-102.

Magnall, J.M., Stern, R.A., Gleeson, S.A., and Paradis, S. (2015) Widespread Euxinic Conditions are not a Prerequisite for Sediment-Hosted Base Metal (Pb-Zn-Ba) Mineralization at MacMillan Pass, Yukon. In S. Paradis, Ed. Targeted Geoscience Initiative 4: Sediment-hosted Zn-Pb deposits: Processes and implications for exploration, p. 43-57. Geological Survey of Canada, Open File 7838.

McLennan, S.M. (1989) Rare-earth elements in sedimentary-rocks: Influence of provenance and sedimentary processes. Reviews in Mineralogy and Geochemistry, 21, 169-200.

Michard, A. (1989) Rare-earth element systematics in hydrothermal fluids. Geochimica et Cosmochimica Acta, 53(3), 745-750.

Morganti, J.M. (1979) The geology and ore deposits of the Howards Pass Area, Yukon and Northwest Territories: The origin of basinal sedimentary stratiform sulphides deposits, p. 351. Unpublished PhD thesis, University of British Columbia.

Norford, B.S., and Orchard, M.J. (1985) Early Silurian age of rocks hosting lead-zinc mineralization at Howards Pass, Yukon Territory and District of Mackenzie. 35 p. Geological Survey of Canada Paper 83-18.

Nozaki, Y., Zhang, J., and Amakawa, H. (1997) The fractionation between Y and Ho in the marine environment. Earth and Planetary Science Letters, 148(1-2), 329-340.

Peter, J.M., and Goodfellow, W.D. (1996) Mineralogy, bulk and rare earth element geochemistry of massive sulphide-associated hydrothermal sediments of the Brunswick Horizon, Bathurst Mining Camp, New Brunswick. Canadian Journal of Earth Sciences, 33(2), 252-283.

Peter, J.M., Goodfellow, W.D., and Doherty, W. (2003) Hydrothermal sedimentary rocks of the Heath Steele belt, Bathurst mining camp, New Brunswick: Part 2. Bulk and rare earth element geochemistry and implications for origin. Economic Geology Monograph, 11, 391-415.

Picard, S., Lecuyer, C., Barrat, J.A., Garcia, J.P., Dromart, G., and Sheppard, S.M.F. (2002) Rare earth element contents of Jurassic fish and reptile teeth and their potential relation to seawater composition (Anglo-Paris Basin, France and England). Chemical Geology, 186(1-2), 1-16.

Pouchou, J.-L., and Pichoir, F. (1991) Quantitative analysis of homogeneous or stratified microvolumes applying the model "PAP". In K. Heinrich, and D. Newbury, Eds. Electron Probe Quantitation, p. 31-75. Plenum Publishing Corporation, New York City, USA.

Pyle, J.M., Spear, F.S., and Wark, D.A. (2002) Electron microprobe analysis of ree in apatite, monazite and xenotime: Protocols and pitfalls. Reviews in Mineralogy and Geochemistry, 48(1), 337-362.

Reed, S. (1990) Fluorescence effects in quantitative microprobe analysis. In D. Williams, P. Ingram, and J. Michael, Eds. Microbeam Analysis, p. 109-114. San Fransisco Press, San Fransisco, USA.

Reynard, B., Lecuyer, C., and Grandjean, P. (1999) Crystal-chemical controls on rare-earth element concentrations in fossil biogenic apatites and implications for paleoenvironmental reconstructions. Chemical Geology, 155(3-4), 233-241.

Reynolds, M.A., Gingras, M.K., Gleeson, S.A., and Stemler, J.U. (2015) More than a trace of oxygen: Ichnological constraints on the formation of the giant Zn-Pb-Ag ± Ba deposits, Red Dog district, Alaska. Geology, 43(10), 867-870.

Rønsbo, J.G. (1989) Coupled substitutions involving REEs and Na and Si in apatites in alkaline rocks from the Ilimaussaq Intrusion, south-Greenland, and the petrological implications. American Mineralogist, 74(7-8), 896-901.

Ruttenberg, K.C., and Berner, R.A. (1993) Authigenic apatite formation and burial in sediments from non-upwelling, continental margin environments. Geochimica et Cosmochimica Acta, 57(5), 991-1007.

Schulz, H.N., and Schulz, H.D. (2005) Large sulfur bacteria and the formation of phosphorite. Science, 307, 416-418.

Shields, G., and Stille, P. (2001) Diagenetic constraints on the use of cerium anomalies as palaeoseawater redox proxies: an isotopic and REE study of Cambrian phosphorites. Chemical Geology, 175(1-2), 29-48.

Simonetti, A., Buzon, M.R., and Creaser, R.A. (2008) In-situ elemental and Sr isotope investigation of human tooth enamel by laser ablation-(MC)-ICP-MS: Successes and pitfalls. Archaeometry, 50(2), 371-385.

Slack, J.F., Falck, H., Kelley, K.D., and Xu, G. (2011) Bottom water redox conditions during Zn-Pb and phosphate mineralization, Howards Pass District, Yukon Territory. Geological Assocation of Canada Abstracts, 34.

Stalder, M., and Rozendaal, A. (2004) Apatite nodules as an indicator of depositional environment and ore genesis for the Mesoproterozoic Broken Hill-type Gamsberg Zn-Pb deposit, Namaqua Province, South Africa. Mineralium Deposita, 39(2), 189-203.

Stock, M.J., Humphreys, M.C.S., Smith, V.C., Johnson, R.D., Pyle, D.M., and Eimf. (2015) New constraints on electron-beam induced halogen migration in apatite. American Mineralogist, 100(1), 281-293.

Stormer, J.C., Pierson, M.L., and Tacker, R.C. (1993) Variation of F-X-ray and Cl-X-ray intensity due to anisotropic diffusion in apatite during electron-microprobe analysis. American Mineralogist, 78(5-6), 641-648.

Sverjensky, D.A. (1984) Europium redox equilibria in aqueous-solution. Earth and Planetary Science Letters, 67(1), 70-78.

Tribovillard, N., Algeo, T.J., Lyons, T., and Riboulleau, A. (2006) Trace metals as paleoredox and paleoproductivity proxies: An update. Chemical geology, 232(1), 12-32.

Trotter, J.A., and Eggins, S.M. (2006) Chemical systematics of conodont apatite determined by laser ablation ICPMS. Chemical Geology, 233(3-4), 196-216.

Turner, R.J. (1992) Formation of Phanerozoic stratiform sediment-hosted zinc-lead deposits: Evidence for the critical role of ocean anoxia. Chemical Geology, 99(1), 165-188.

Wheat, C.G., Feely, R.A., and Mottl, M.J. (1996) Phosphate removal by oceanic hydrothermal processes: An update of the phosphorus budget in the oceans. Geochimica et Cosmochimica Acta, 60(19), 3593-3608.

Wright, J., Schrader, H., and Holser, W.T. (1987) Paleoredox variations in ancient oceans recorded by rare earth elements in fossil apatite. Geochimica et Cosmochimica Acta, 51(3), 631-644.

Xiao, S.H., Zhou, C.M., Liu, P.J., Wang, D., and Yuan, X.L. (2014) Phosphatized acanthomorphic acritarchs and related microfossils from the Ediacaran Doushantuo Formation at Weng'an (South China) and their implications for biostratigraphic correlation. Journal of Paleontology, 88(1), 1-67.

Figure Captions

Figure 1: A) Simplified geology map of the Selwyn basin showing locations of the major SEDEX districts, B) Geological map of the Howard's Pass district, showing locations of SEDEX deposits (modified from Goodfellow, 2007; Gordey and Anderson, 1993)

Figure 2: A) Stratigraphic section of the Howard's Pass district. Note that the Zn-Pb SEDEX deposits are hosted entirely within the ACTM, whereas phosphatic mudstone occurs in the CCMS, ACTM and USMS (modified from Gordey and Anderson, 1993); B) Bedded phosphatic, carbonaceous mudstone with small calcite nodules and minor pyrite; n: nodular carbonate.

Figure 3: BSE images of apatite textures, A) Bedded apatite with interstitial quartz, calcite and organic carbon from the USMS (sample Don-223-23.1); note: dashed white lines indicate boundaries between apatite bed and adjacent (intercalated) carbonaceous mudstone, B) Bedded apatite replacing acritarch microfossils (white arrows) within cherty carbonaceous USMS; note LA-ICP-MS spot analyses (red spot with black outline) (sample XYC-190-286.2); C) Bedded and granular bedded subhedral apatite with interstitial quartz, calcite, organic carbon and pyrite within ACTM (sample XYC-224-184.0); D) Bedded granular to partially recrystallized apatite partially replacing organic carbon in USMS (sample XYC-224-116.8); E) Minute apatite nodules (nod) and apatite partially replacing organic carbon (C_{org}) of acritarch microfossils (fos) in cherty carbonaceous matrix from the USMS (sample XYC-224-116.8); F) Subhedral

microcrystalline apatite partially replacing organic carbon (C_{org}) of acritarch microfossils in calcite-rich matrix from the ACTM (sample XYC-190-416.3).

Figure 4: North American shale composite-normalized (Gromet et al., 1984) REE-Y plots of A) Average LA-ICP-MS analyses of apatite from the HPD; B) Whole-rock phosphatic mudstone (HPD), LA-ICP-MS CFA laminae (HPD), Upper Ordovician phosphorite from southeast Missouri and Early Silurian from central New York (Emsbo et al., 2015); C) Average of igneous Durango fluorapatite (this study), hydrothermal apatite from Heath Steele belt Fe formation, Canada (Peter et al., 2003), Sn-W vein mineralization Panasqueira, Portugal (Knutson et al., 1985) and low temperature hydrothermal apatite from an equatorial Pacific seamount (Hein et al., 1993). Note: REE arranged in order of decreasing effective atomic radii in trivalent state and octahedral coordination and, because of this arrangement, Y is inserted between Dy and Ho (Bau and Dulski, 1996).

Figure 5: Bivariate plot of $(La/Sm)_N$ vs. $(La/Yb)_N$ for apatite analyzed by LA-ICP-MS. The modern seawater field and trajectories for early diagenesis (adsorption), late diagenesis (recrystallization) and substitution are from (Reynard et al., 1999).

Figure 6: Bivariate plot of NASC-normalized Ce/Ce* vs. Pr/Pr* for apatite analyzed by LA-ICP-MS. Field I: nil Ce* and nil La* anomalies; Field IIa: positive La* anomaly, nil Ce* anomaly; Field IIb: negative La* anomaly, nil Ce* anomaly; Field IIIa: positive Ce* anomaly; Field IIIb: negative Ce* anomaly (fields from Bau and Dulski, 1996). See text for further explanation of the fields.

5550 Gadd et al. Fig. 1

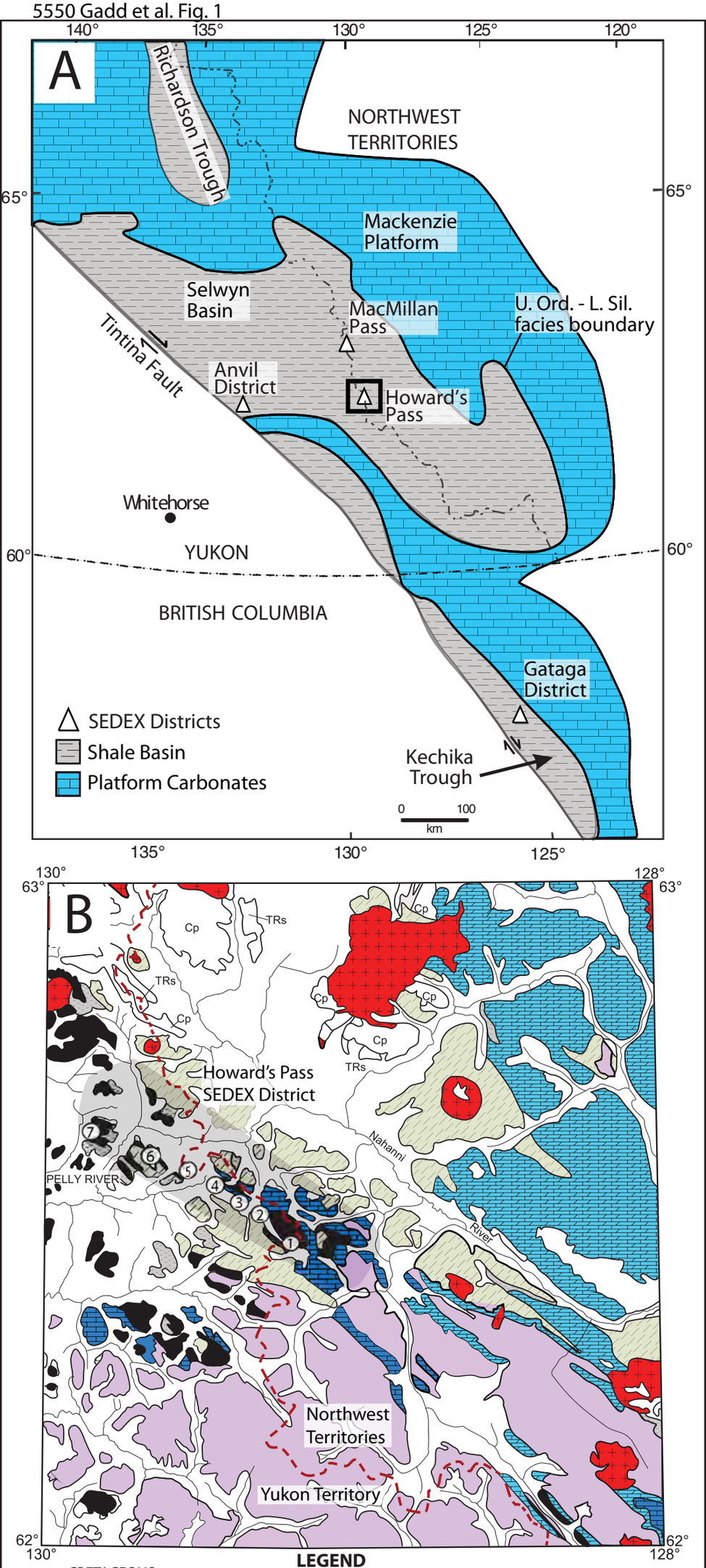

5550 Gadd et al. Fig. 2

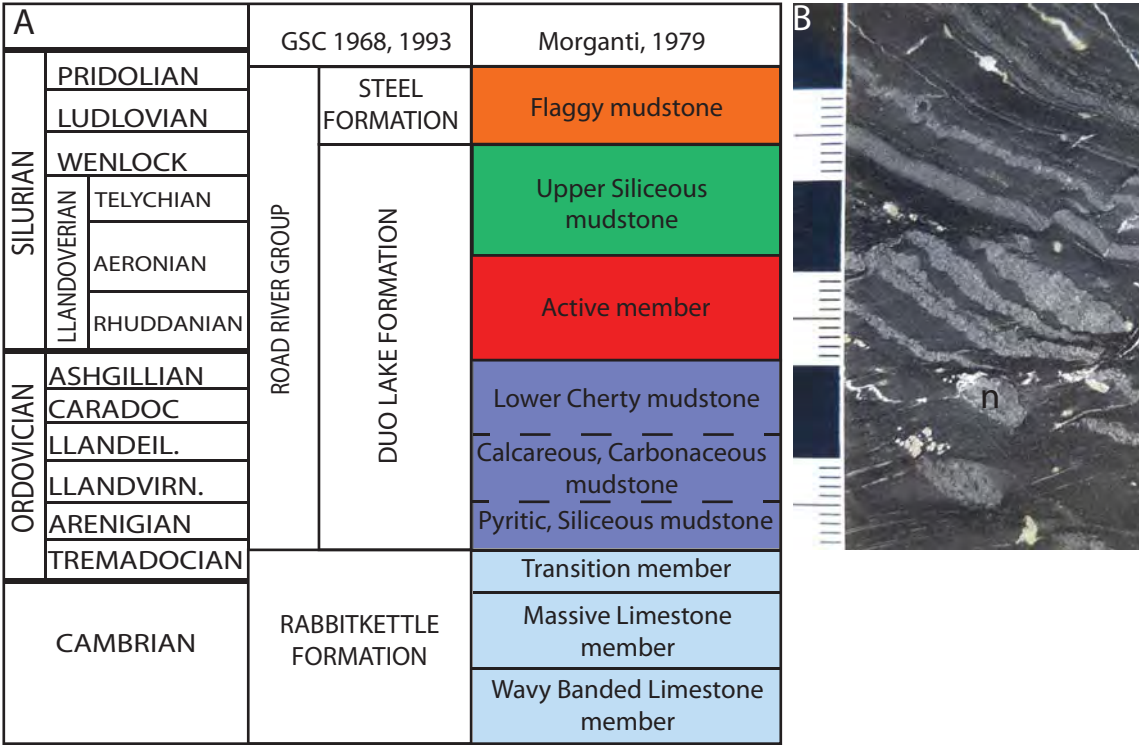

5550 Gadd et al. Fig. 3

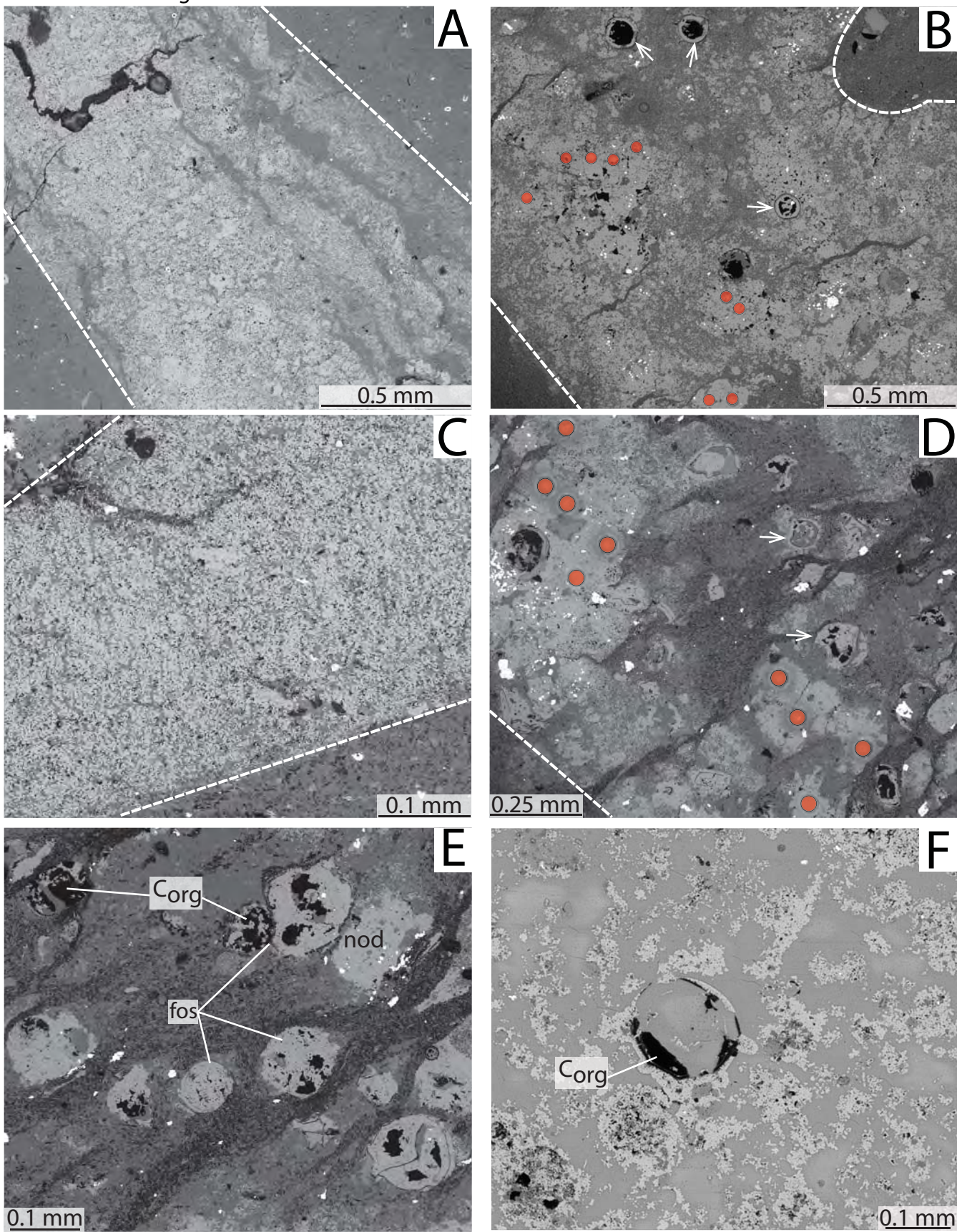

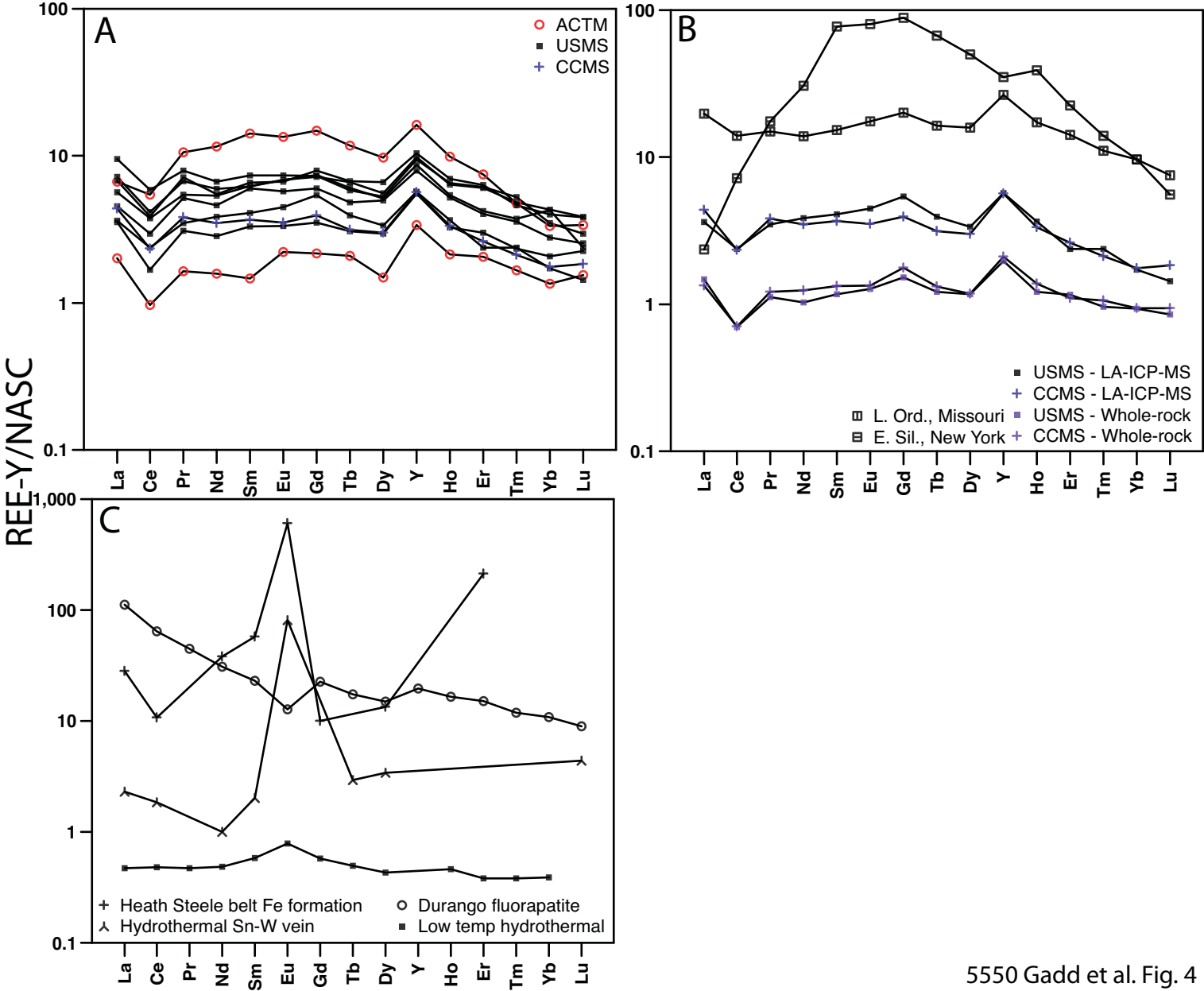

5550 Gadd et al. Fig. 4

5550 Gadd et al. Fig. 5

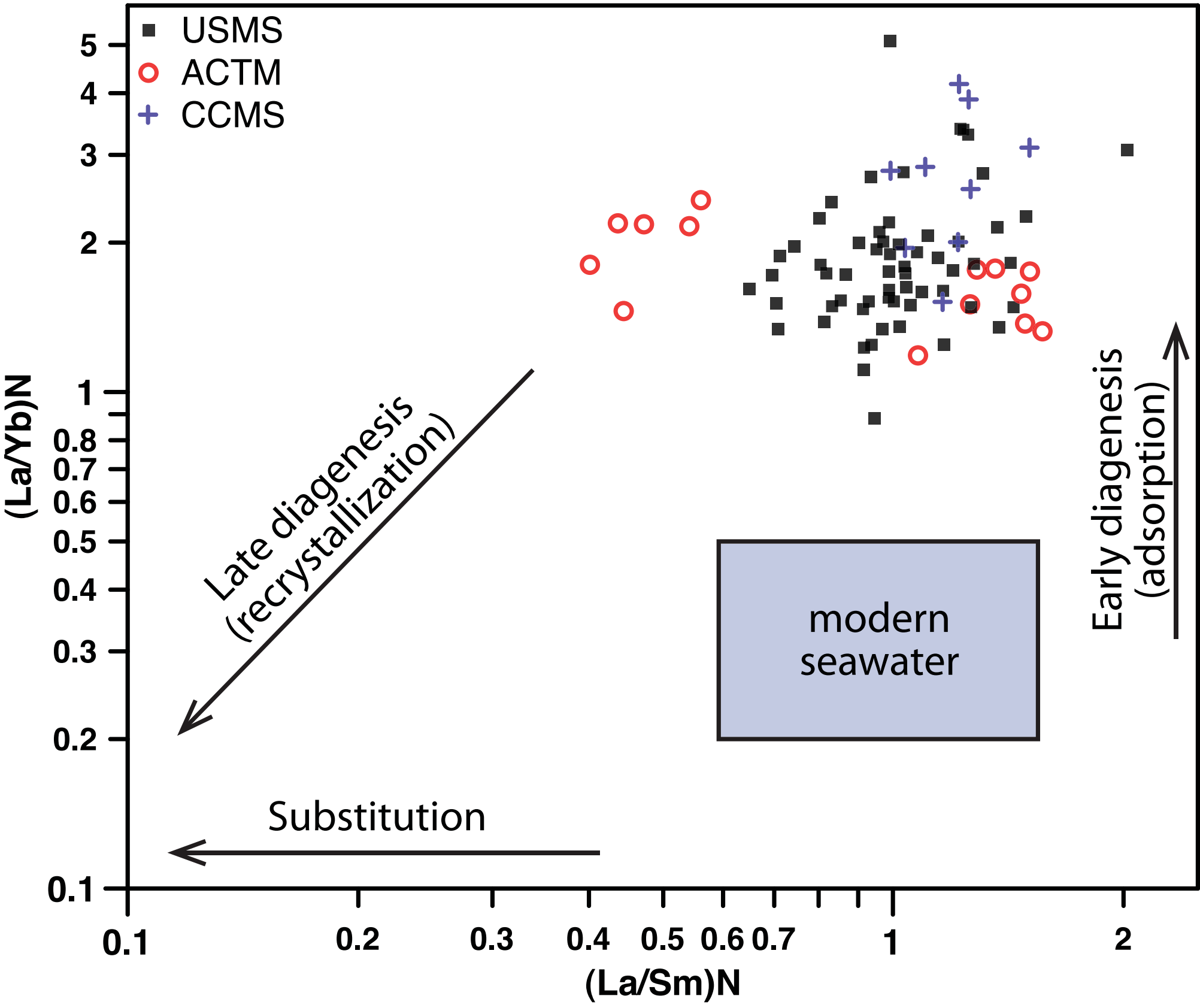

5550 Gadd et al. Fig. 6